The Canadian Mineralogist
Vol. 58, pp. 829-845 (2020)
DOI: 10.3749/canmin.1900084

BERYLLIUM-SILICON DISORDER AND RARE EARTH CRYSTAL CHEMISTRY IN GADOLINITE FROM THE WHITE CLOUD PEGMATITE, COLORADO, USA

Julien M. ALLAZ[§,*], Joseph R. SMYTH, Rhiana E. HENRY[†], and Charles R. STERN

Department of Geological Sciences, University of Colorado, 2200 Colorado Avenue, Boulder, Colorado 80309, USA

Philip PERSSON

Department of Geology, Colorado School of Mines, 1516 Illinois Street, Golden, Colorado 80401, USA

Joy J. MA and Markus B. RASCHKE

Department of Physics, Department of Chemistry, and JILA, University of Colorado, 2000 Colorado Avenue, Boulder, Colorado 80302, USA

Abstract

Gadolinite, $REE_2FeBe_2Si_2O_{10}$, is a monoclinic orthosilicate member of the gadolinite supergroup of minerals and occurs in beryllium and rare earth element (REE) bearing granites, pegmatites, and some metamorphic rocks. Gadolinite from the White Cloud pegmatite, South Platte Pegmatite district, Colorado, USA, has been investigated and shows unusually variable REE compositions and distinct Be-Si disorder. Crystal structure and chemistry of two petrographically distinct gadolinite samples from this locality have been studied by electron microprobe chemical analysis, laser ablation inductively coupled plasma-mass spectrometry (LA-ICP-MS), single-crystal X-ray diffraction (XRD), and micro-Raman spectroscopy. Within these samples, the gadolinite was found to range from gadolinite-(Y) to gadolinite-(Ce). Regions of nearly full occupancy of Fe at the M site, and partial substitution of Si for Be at the Q tetrahedral site, as well as substitution of Be for Si at the T site were observed, with up to 15% vacancy at the Fe site and up to 15% disorder between Be and Si at distinct tetrahedral sites elsewhere. The layered nature of the crystal structure allows for large variation of the radius of the cation at the A site which contains the REE. This study shows that Be may substitute for Si and that Be may be more abundant in geochemical systems than previously assumed.

Keywords: gadolinite, rare earth elements, beryllium, structural disorder, single crystal X-ray diffraction, electron microprobe, Raman spectroscopy.

Introduction

The gadolinite supergroup is a group of structurally related minerals with general chemical formula $A_2MQ_2T_2O_8\varphi_2$, with principal cations A = Ca, REE; M = Fe, Ca, □ (vacancy); Q = Be, B; T = Si, P, As; and φ = O, OH, F, and with a monoclinic unit cell with space group $P2_1/c$ (Bačík *et al*. 2017 and references therein). Of the specific species gadolinite $REE_2FeBe_2Si_2O_{10}$, three sub-species have been distinguished depending on the major REE: gadolinite-(Ce) (Segalstad & Larsen 1978), gadolinite-(Y) (Miyawaki *et al*. 1984), and gadolinite-(Nd) (Škoda *et al*. 2016, 2018). Although usually considered an orthosilicate, gadolinite has a layered crystal structure, with sheets of crystallographically distinct Be (Q) and Si (T) tetrahedra forming four- and eight-membered rings of alternating Si^{4+} and Be^{2+} tetrahedra (Fig. 1).

§ *Corresponding author e-mail address*: julien.allaz@erdw.ethz.ch
* Present address: ETH Zürich, Department of Earth Sciences, Institute of Geochemistry and Petrology, Clausiusstrasse 25, 8092 Zürich, Switzerland.
† Present address: University of British Columbia, Department of Earth, Ocean, and Atmospheric Sciences, 2020 – 2207 Main Mall,Vancouver, BC, V6T 1Z4, Canada.

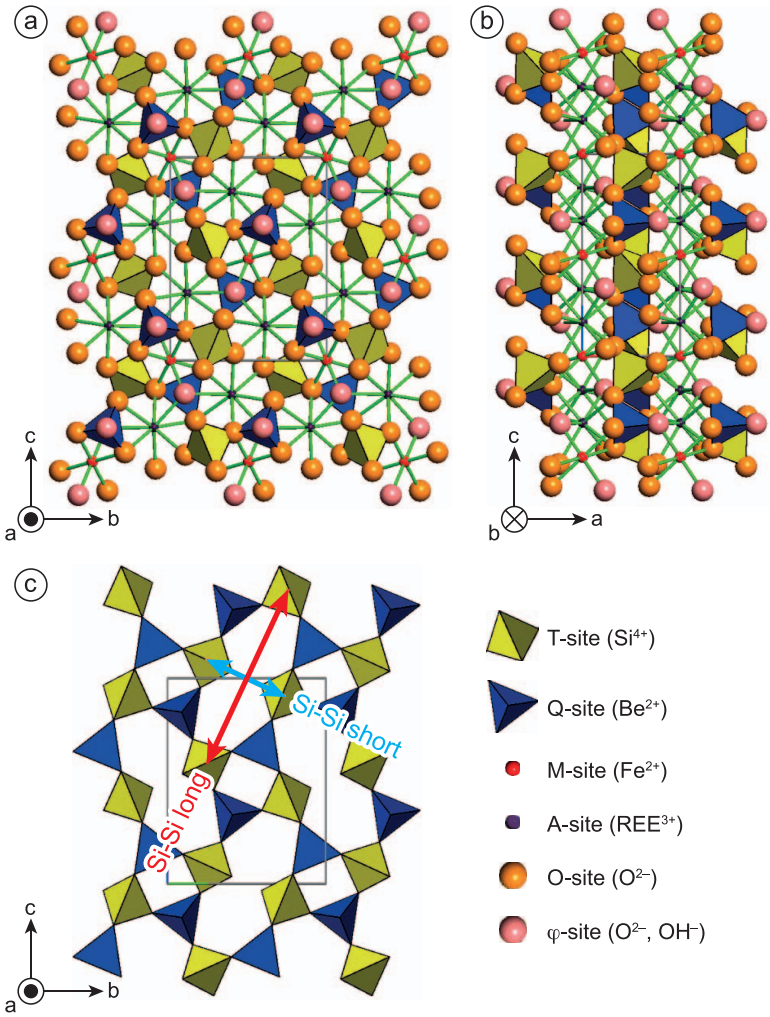

FIG. 1. Crystal structure of gadolinite-(Y). (a) Top view of the (100) sheet. (b) Perpendicular to the (100) sheet. (c) TO_4 and QO_4 tetrahedra in alternating eight- and four-membered rings.

Between the sheets of tetrahedra, there is an interlayer of REE^{3+} at eight-coordinated A sites and Fe^{2+} at octahedrally coordinated M sites. There are four distinct oxygen sites (O1–O4) plus a φ anion site, all occupied by O in gadolinite (Fig. 1a, b). All atoms are at general positions in $P2_1/c$ so there are four of each per unit cell, except M, which is at a special position at the origin so there are two per unit cell.

Gadolinite commonly shows solid solution towards the isostructural hingganite, $REE_2\square Be_2Si_2O_8(OH,F)_2$ and datolite, $Ca_2\square B_2Si_2O_8(OH,F)_2$. In solid solution with hingganite or datolite, the octahedral M site of gadolinite becomes partially vacant, with charge compensation *via* hydroxylation of the φ site. In solid solution with datolite, there is an additional coupled substitution of Be^{2+} for B^{3+} and REE^{3+} for Ca^{2+}. As divalent Ca has a larger ionic radius than most trivalent REE cations (with the exceptions of La^{3+}, Ce^{3+}, and Pr^{3+}), the eight-membered tetrahedral ring widens (Fig. 1c) so that the Si–Si short distance increases. Gadolinite subgroup minerals tend to have a longer Si–Si long distance than the datolite subgroup (Bačík *et al.* 2014). The tetrahedral rings display a negative correlation between short and long Si–Si distances for gadolinite group minerals. The Si–Si long distance is correlated with the occupancy of the T site, whereas the occupancies of the A and M sites are

correlated with the Si–Si short distance (Bačík *et al*. 2014).

Gadolinite is commonly found in granite pegmatites (*e.g*., Nilssen 1973, Pezzotta *et al*. 1999, Černý & Ercit 2005, Bačík *et al*. 2014). Despite its significant presence in the White Cloud pegmatite, South Platte pegmatite district within the Pikes Peak granite in Colorado, USA (Haynes 1965, Simmons & Heinrich 1980), there has been only limited characterization of gadolinite from this locality. The goal of the present study is to place gadolinite from this occurrence within the context of the recently refined spectrum of gadolinite-group crystal chemistry (Bačík *et al*. 2014, 2017). Using a combination of electron microprobe (EMP) analysis, laser ablation inductively coupled plasma mass spectrometry (LA-ICP-MS), single crystal X-ray diffraction (XRD), and micro-Raman spectroscopy, the Be-Si disorder in gadolinite is characterized and the crystallographic distortion due to compositional variation from light REE-rich (LREE: La to Eu) to Y + heavy REE-rich (HREE: Gd to Lu) species is discussed.

Geological Setting

The White Cloud pegmatite is part of the South Platte pegmatite district (Haynes 1965, Simmons & Heinrich 1980), which is hosted within the Proterozoic anorogenic "A-type" Pikes Peak granite (Smith *et al*. 1999). This pegmatite district spans 80 km^2 and contains over 50 decameter-sized pegmatites concentrated in the north end of the batholith. The South Platte pegmatites are well known for their local concentrations of REE minerals, suggesting an REE enrichment, and depletion in boron, as suggested by the absence of tourmaline. Many of these pegmatites are concentrically zoned, with a border zone of graphic granite enriched in biotite, a K-feldspar-rich intermediate domain, and a quartz-rich core. The White Cloud pegmatite is ~100 × 40 m, and the REE-rich phases are concentrated in pods and veins at the interface between the intermediate microcline-rich zone and the quartz core. This mineralization consists of several REE-rich minerals including allanite-(Ce), gadolinite-(Ce,Y), thalénite-(Y), REE-carbonates, and fluocerite. Gadolinite appears to occur throughout all REE mineral-bearing zones of the White Cloud pegmatite and seems concentrated in two main assemblages. The first assemblage (sample SWC) is most abundant and consists of a fluorite-rich mass up to ~3 m across composed of green to purple anhedral fluorite and quartz, which hosts relatively abundant disseminated anhedral gadolinite grains 2–5 mm in size (up to ~3 cm) and associated with REE carbonates and minor allanite-(Ce). The second assemblage (sample Z2A) occurs as veins and pods up to ~2 m in maximum dimension composed of quartz, microcline, fluorite, thalénite-(Y), allanite-(Ce), REE-carbonates, and subordinate euhedral to subhedral gadolinite. These two assemblages are spatially separate but do occur in relatively close proximity (~10 m apart) to each other along the N/NE perimeter of the core-intermediate zone contact of the White Cloud pegmatite. Much of the core and significant quantities of the REE zone have been mined, so the original extent and continuity of the REE mineral-bearing zones is largely unknown (Simmons & Heinrich 1980).

Sample Description

Two thin sections, SWC and Z2A, were used for the EMP and micro-Raman spectroscopic analyses (Fig. 2). An additional thin section, WC1-A, was prepared for additional petrographic studies and complementary *in situ* analyses; this additional sample is an equivalent of sample Z2A. Gadolinite in SWC is a rounded centimeter-sized olive-green mass, associated with fluorite, feldspar, and quartz, with dark brown allanite-(Ce) inclusions. Simmons & Heinrich (1980) described a close association of gadolinite and allanite-(Ce) and a dark reddish brown bastnäsite-(Ce) rim resulting from the alteration of REE-silicate minerals. The investigated samples do not display such a bastnäsite rim, and only scarce REE-carbonates are found locally along the rim or within cracks. In sample Z2A, the gadolinite crystals are 1–4 mm across in a matrix of fluorite and are surrounded by allanite-(Ce), thalénite-(Y), and synchysite-(Y). All of the gadolinite crystals show an oscillatory zonation visible in cross-polarized light (Fig. 2f, h). Sample Z2A is more homogeneous, with less optical variation.

Methods

Single crystal X-ray diffraction

Crystal chips of *ca*. 100 μm diameter were extracted using a micro-drill from samples SWC and Z2A and were prepared for single-crystal XRD. For both samples, care was taken to extract a crystal chip showing minimal compositional variation, as ascertained by EMP analyses. The XRD analyses were conducted at the University of Colorado, Boulder, using a Bruker *P*4 four-circle diffractometer with an APEX II CCD detector and a rotating Mo-anode generator. The Mo-anode generator was operated at 50 kV and 250 mA with a graphite monochromator. Sample SWC was analyzed through 2θ of 70°, and Z2A was analyzed through 2θ of 80°. Atom positions, anisotropic displacement parameters, and site occupancy were

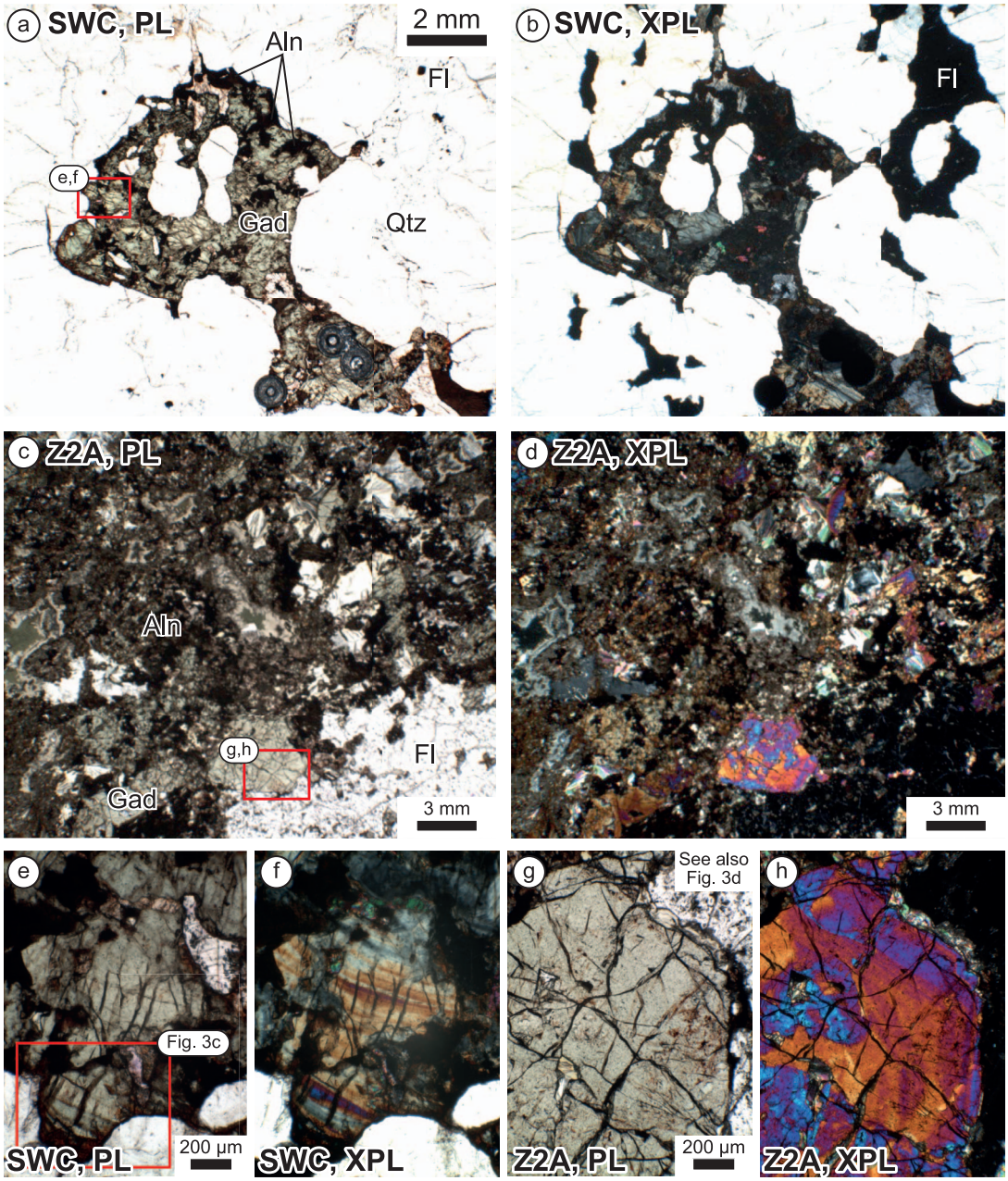

FIG. 2. Microphotographs of gadolinite minerals in samples SWC (a, b, e, f) and Z2A (c, d, g, h). PL: plane-polarized light, XPL: cross-polarized light. Aln = allanite, Gad = gadolinite, Fl = fluorite, Qtz = quartz. Note the oscillatory zoning clearly visible optically in (f) and (h).

refined for each specimen using SHELXL Version 2016/4 (Sheldrick 2015) in the WinGX-2014 software package (Farrugia 2014). Ionized-atom scattering factors were used for refinements (Cromer & Mann 1968, Azavant & Lichanot 1993). The A-site cation occupancies were refined using a Yb^{3+} scattering factor because it has a high atomic number. The structural occupancy appears low since the number of electrons

detected for a mix of REE and Y is less than that for pure Yb. The M-site occupancy was refined using the Fe^{2+} scattering factor. Both Si and Be were allowed to occupy the T and Q sites. The oxygen sites were fixed at full occupancy (5 O, $Z = 2$) and allowed to vary spatially. Twinning instructions were included in the SHELXL refinement consistent with those of Cámara *et al*. (2008). The *R*-factor improved with the twin matrix applied to the refinement, although the twin fraction refined to less than one percent in both refinements.

Raman spectroscopy

Micro-Raman spectroscopy and imaging of thin sections of SWC and Z2A were performed in the Nano-Optics Laboratory, University of Colorado-Boulder, using a specially designed homebuilt confocal Raman microscope (based on an upright Olympus BX51 microscope, with an Olympus MPlanFL N 50×/0.80NA BD objective, and a Princeton Instruments Acton SpectraPro SP2500 spectrograph, with liquid nitrogen-cooled CCD camera). The Raman spectra were collected in epi-illumination using 632.8 nm He-Ne laser light, with 20 mW, focused onto the sample. Spectral resolution is 3.0 cm^{-1} (full width at half maximum) with a 600 lines/mm grating and a confocal pinhole. Helium and Ne lamp emission lines were used for calibration. Individual point spectra and arrays were acquired from 50 to 4000 cm^{-1} with 50 s acquisition time per pixel. The arrays were acquired using a P-545.xR8S PInano XYZ Piezo scanner with 10 μm step size.

Electron microprobe

The EMP analyses and backscattered electron (BSE) images were collected with a JEOL JXA-8230 microprobe at the University of Colorado-Boulder. The instrument is equipped with five WDS spectrometers, four of which are equipped with large-area monochromators, and a 10 mm^2 Thermo UltraDry EDS. The EDS detector was used to identify the mineral assemblage and the major compositional variations within individual crystals. In parallel, BSE imaging of SWC and Z2A was used to identify zonation within the gadolinite and to select regions for quantitative analyses in order to capture the compositional variability. All analyses were collected with an acceleration voltage of 15 keV, a 20 nm carbon coating, and using the software *Probe for EPMA*. For the largest homogeneous domains, a 5 μm defocused beam at 50 nA current was used to prevent beam damage. For smaller domains, the current was decreased to 30 nA and the beam was defocused to 2 μm. All analyses were acquired using the Mean Atomic Number (MAN) background correction (Donovan & Tingle 1996). No beam damage was observed during the four-minute analysis at these conditions. Additional analytical details and a list of standards used is given in Table 1. In addition to the analysis of thin sections, the crystal chip of sample SWC was mounted on a glass slide after the XRD and polished for additional EMP analysis to confirm the composition. Micro-Raman spectroscopy was performed after EMPA and carbon removal on the selected regions of samples Z2A and SWC.

Laser ablation-inductively coupled plasma-mass spectrometry

Lithophile trace elements, Be, and B concentrations in gadolinite were measured for sample WC-1A with laser ablation sector field ICP-MS (LA-ICP-MS) at the Institute of Geochemistry and Petrology, ETH Zürich. Details of the analytical instruments are described in Guillong *et al*. (2014). Ablation times were 30 s for individual measurements at energies of 2J/cm^2 and repetition rates of 4Hz, using a laser spot size of 19μm. NIST610 was used as a primary reference material and GSD-1G was used as validation reference material with identical ablation conditions as the sample. The EPMA measurements of Y obtained from the same spot were used for internal standardization. The results are given in Supplementary Table 2[1].

Results

X-ray diffraction

The crystal structure refinement yielded a monoclinic unit cell with space group $P2_1/c$, with parameters displayed in Table 2. The cell parameters of SWC are significantly larger than those of Z2A. Selected nearest-neighbor distances are listed in Table 3. The φ site is included in the nearest neighbor distances as an oxygen atom, based on the assumption of 10 oxygen atoms per formula unit. The refined atomic positions and displacement parameters are listed in Table 4. The refined occupancies of various sites are given in Table 5. The small amount of water (see Raman below) was neglected for the structure refinement. However, considering the presence of numerous heavy elements in gadolinite, the presence or absence of minor amounts of H in the φ site does not affect the refinement results. Significant positive residuals were observed near the A sites in both refinements. This is not unexpected for a site with a large number of different chemical substituents. Atom fragments were added to these

[1] Supplementary Data are available from the Depository of Unpublished Data on the MAC website (http://mineralogicalassociation.ca/), document "Gadolinite, CM58, 19-00084".

TABLE 1. ANALYTICAL CONDITIONS AND STANDARDS USED FOR EMP ANALYSES

Element	Crystal	Standard	Pos. (mm)	t_{Peak} (s) *	DL †	Interferences
Y *Lα*	TAP 1	YPO_4	70.14	60	140–200	Si
Si *Kα*	TAP 1	Amelia Albite	77.45	30	65–85	Ho, Tm, Yb, Y
Mg *Kα*	TAP 1	Diopside	107.48	90	40–60	Tb, Eu, Nd, Dy
Al *Kα*	TAP 1	Almandine NY	90.63	90	35–55	Tm, Ho, Yb, Er
Th *Mα*	PETL 2	ThO_2	132.41	90	210–270	-
U *Mβ*	PETL 2	UO_2	118.88	90	170–220	Th
Ca *Kα*	PETL 2	Fluorapatite	107.48	90	25–35	Yb, Dy
Pb *Mβ*	PETL 3	Pyromorphite	162.55	300	100–135	Ce
La *Lα*	LIFL 4	$LaPO_4$	185.38	40	265–350	Nd
Ce *Lα*	LIFL 4	$CePO_4$	178.14	40	240–315	-
Nd *Lα*	LIFL 4	$NdPO_4$	164.84	40	220–290	Ce
Pr *Lβ*	LIFL 4	$PrPO_4$	157.09	40	400–530	-
Sm *Lβ*	LIFL 4	$SmPO_4$	138.98	40	420–550	Tb, Er
Tb *Lα*	LIFL 4	$TbPO_4$	137.42	40	245–325	Sm, Pr, Tm
Eu *Lβ*	LIFL 4	$EuPO_4$	133.58	40	430–570	Dy
Dy *Lα*	LIFL 5	$DyPO_4$	132.68	30	260–345	Eu, Yb, Sm
Gd *Lβ*	LIFL 5	$GdPO_4$	128.34	30	470–625	Ho
Er *Lα*	LIFL 5	$ErPO_4$	124.01	40	240–315	Tb, Eu
Yb *Lα*	LIFL 5	$YbPO_4$	116.14	40	265–355	Dy, Eu, Tb, Sm
Ho *Lβ*	LIFL 5	$HoPO_4$	114.44	40	475–625	Eu, Sm, Dy
Tm *Lα*	LIFL 5	$TmPO_4$	119.97	40	255–340	Dy, Sm, Tb
Fe *Kα*	LIFL 5	Almandine NY	134.56	20	115–150	Dy, Eu, Nd, Sm
Lu *Lα*	LIFL 5	$LuPO_4$	112.47	40	285–380	Dy, Ho

* Only a peak measurement was acquired, as the MAN background correction was used (Donovan & Tingle 1996). See Allaz *et al.* (2019) for a comparison of multipoint-background and MAN background acquisitions.
† DL = detection limit in ppm.

positions in the final stages of refinement, which significantly reduced the final *R* values. The XRD structural refinements converged to an *R* value of 0.049 for SWC and 0.053 for Z2A. These are robust refinements for a chemically complex structure. Gibson & Ehlmann (1970) demonstrated that metamict gadolinite crystals give poor diffraction patterns. However, the White Cloud gadolinite minerals are all low in actinide contents (see below) and do not appear to have sufficient radiation damage to affect the refinements.

TABLE 2. X-RAY DIFFRACTION DATA AND REFINEMENT PARAMETERS FOR GADOLINITE SAMPLES

Parameter	SWC	Z2A
a (Å)	4.8201(2)	4.7770(9)
b (Å)	7.6883(3)	7.5604(21)
c (Å)	10.1347(5)	10.0166(24)
β (°)	90.009(3)	90.402(12)
Volume (Å^3)	375.58	361.75
2θ Max (°)	70.2	80.7
# Reflections	10761	9938
#Unique Reflections	1607	2158
R(int)	0.047	0.054
R	0.048	0.049

Raman spectroscopy

Representative Raman spectra for samples SWC and Z2A are shown in Figure 3a–b. The bands between 200 and 750 cm^{-1} are due to bending modes of Si–O and Be–O, stretching vibrations of REE–O and Fe–O, and other lattice vibrations (Škoda *et al.* 2016). Both samples have their most prominent peak between 900 and 914 cm^{-1} and a minor peak around 980 cm^{-1}. These peaks are attributed to stretching vibrations of Be–O and Si–O in tetrahedral coordination (Škoda *et al.* 2016), similar to phenakite (Be_2SiO_4). The weak spectral features in the 3000 to 3600 cm^{-1} region correspond to different OH-stretching vibrations of water. The underlying background in the 2900–4000 cm^{-1} region is due to fluorescence with considerable spatial variability.

Raman hyperspectral imaging was performed on samples SWC and Z2A across regions with varying

TABLE 3. SELECTED NEAREST NEIGHBOR DISTANCES, POLYHEDRAL VOLUMES, QUADRATIC ELONGATION, ANGLE VARIANCE, AND ELECTRON OCCUPANCIES FOR CATION SITES IN GADOLINITE SAMPLES

A site	SWC	Z2A
A–O1 (Å)	2.385(5)	2.346(4)
A–O1 (Å)	2.388(5)	2.320(4)
A–O2 (Å)	2.452(4)	2.411(3)
A–O3 (Å)	2.730(5)	2.478(4)
A–O3 (Å)	2.547(5)	2.694(4)
A–O4 (Å)	2.450(4)	2.413(4)
A–φ (Å)	2.536(5)	2.384(4)
A–φ (Å)	2.432(5)	2.496(4)
<A–O> (Å)	2.490	2.443
Polyhedral Volume (Å^3)	26.3(4)	24.7(2)
Electrons at Site	46.2(4)	43.6(3)
M site	**SWC**	**Z2A**
M–O2(2) (Å)	2.324(5)	2.289(4)
M–O4(2) (Å)	2.227(5)	2.203(4)
M–φ(2) (Å)	2.050(5)	2.049(4)
<M–O> (Å)	2.201	2.180
Polyhedral Volume (Å^3)	13.2(2)	12.9(1)
O. Q. E.	1.052	1.048
Angle Variance	162.2	154.8
Electrons at Site	21.1(3)	22.7(2)
Q site	**SWC**	**Z2A**
Q–O2 (Å)	1.668(7)	1.648(6)
Q–O3 (Å)	1.679(7)	1.667(6)
Q–O4 (Å)	1.648(8)	1.654(7)
Q–O5 (Å)	1.598(8)	1.594(6)
<Q–O> (Å)	1.648	1.641
Polyhedral Volume (Å^3)	2.27(5)	2.23(4)
T. Q. E.	1.0090	1.0105
Angle Variance	41.4	48.1
Electrons at Site	2.78(15)	2.49(10)
T site	**SWC**	**Z2A**
T–O1 (Å)	1.606(5)	1.602(4)
T–O2 (Å)	1.646(5)	1.649(4)
T–O3 (Å)	1.631(5)	1.618(4)
T–O4 (Å)	1.654(5)	1.649(4)
<T–O> (Å)	1.634	1.629
Polyhedral Volume (Å^3)	2.23(3)	2.21(2)
T. Q. E.	1.0028	1.0045
Angle Variance	11.6	18.3
Electrons at Site	8.70(16)	9.40(11)

heavy REE (HREE = Y + Gd to Lu) and light REE (LREE = La to Eu) contents, as identified with EMP analysis (BSE images in Fig. 3c, d of locations indicated in Fig. 4c, d). The BSE images are correlated with images of values of Raman peak position $\tilde{\nu}$ (top panel) and spectral linewidth Γ (middle panel) obtained for the tetrahedral Be–O stretching vibration between 900 and 914 cm^{-1}, from spectral fits to Lorentzian and Voigt line shapes (Fig. 3c–d). A distinct increase in linewidth correlated with spectral red-shift is observed and associated with the spatial variation in LREE *versus* HREE content, except in a certain region of sample SWC (Fig. 3 c, e) that seems structurally more disordered. A larger linewidth and more pronounced red-shift in SWC compared to Z2A suggest greater disorder, which we attribute to the increased Be–Si disorder as well as higher amounts of Th in sample SWC.

Electron microprobe analysis

The variation of BSE intensity correlates with low-density domains rich in Y+HREE and brighter high-density domains rich in LREE (Fig. 4). The zoning is particularly prominent in one exceptionally large agglomerate of euhedral to subhedral gadolinite crystals in sample WC1-A (Fig. 4a), with core domains rich in LREE and rims richer in HREE. Some core domains appear patchy (Fig. 4d, e). Oscillatory zonation with alternation of Ce-rich and Y-rich domains is present in all samples (Fig. 4a, c, e). Rare REE-carbonates and Fe-oxides are present in cracks in a few grains (Fig. 4b). The edges of some grains show some minimal alteration (Fig. 4c). Sample Z2A is (Y+HREE)-rich and more homogeneous than SWC, with a slight increase in HREE towards the edges of the crystals (Fig. 4e).

The EMP analyses were obtained from thin sections of samples SWC and Z2A, and from the grain mount of SWC. Representative average analyses and corresponding atoms per formula unit values in high- and low-density regions are given in Table 6. The gadolinite formula was first normalized to 10 oxygen anions, and the Be content was recalculated by further assuming 4 *apfu* of Si + Be and no hingganite or datolite component (*i.e.*, no hydroxylation of the φ site). In contrast, the simpler constraint of 2 *apfu* of Be appears inaccurate, as both the EMP and the XRD results suggest an excess of Si in some samples (see discussion below). Based on this first normalization, analyses from sample SWC tend to yield an abnormally low M-site occupancy, which suggests the presence of vacancies and a substitution towards hingganite or datolite. Since the B content is very low (as determined by LA-ICP-MS, see below), we

TABLE 4. ATOMIC POSITION, DISPLACEMENT PARAMETERS, AND ELECTROSTATIC ENERGIES FOR GADOLINITE SAMPLES

SWC	*x*	*y*	*z*	*U*11	*U*22	*U*33	*U*23	*U*13	*U*12	Electrostatic Potential (V)
A(REE)	0.99856(8)	0.10804(6)	0.32796(4)	0.0139(2)	0.0146(2)	0.0112(2)	0.0012(1)	0.0018(1)	–0.0003(2)	–29.39
M(Fe)	0.0	0.0	0.0	0.0117(7)	0.0272(9)	0.0099(7)	0.0058(5)	–0.0002(4)	–0.0007(6)	–23.70
Q(Be)	0.5331(12)	0.4136(8)	0.3365(6)	0.014(4)	0.017(7)	0.013(3)	0.001(2)	–0.001(2)	0.001(2)	–30.94
T (Si)	0.4793(4)	0.2730(2)	0.07892(17)	0.0087(8)	0.0090(9)	0.0049(8)	–0.0015(5)	0.0002(5)	–0.0004(6)	–48.41
O1	0.2424(9)	0.4087(6)	0.0324(4)	0.015(2)	0.020(2)	0.016(2)	0.0024(17)	–0.0022(2)	–0.0039(18)	25.74
O2	0.6711(9)	0.2877(6)	0.4533(4)	0.013(2)	0.017(2)	0.013(2)	0.0034(15)	0.0032(14)	0.0022(16)	27.13
O3	0.6826(9)	0.3458(6)	0.1959(4)	0.015(2)	0.024(2)	0.009(2)	–0.0052(15)	0.0000(13)	–0.0045(17)	26.56
O4	0.3167(10)	0.1035(6)	0.1395(4)	0.018(2)	0.0119(18)	0.017(2)	0.0007(16)	0.0033(15)	–0.0052(17)	27.54
ϕ (O5)	0.2016(10)	0.4123(7)	0.3348(4)	0.013(2)	0.025(2)	0.016(2)	–0.0014(17)	–0.0017(15)	0.0014(18)	22.80
Z2A	*x/a*	*y/b*	*z/c*	U11	U22	U33	U23	U13	U12	Electrostatic Potential (V)
A(REE)	0.00027(7)	0.10748(5)	0.32856(4)	0.00977(13)	0.01366(17)	0.01250(14)	–0.00101(9)	0.00053(9)	–0.00017(9)	–30.15
M(Fe)	0.0	0.0	0.0	0.0078(4)	0.0224(6)	0.0117(5)	0.0043(4)	–0.0011(3)	0.0000(4)	–23.85
Q(Be)	0.5346(11)	0.4130(8)	0.3349(5)	0.001(2)	0.016(3)	0.014(2)	0.001(2)	–0.0006(16)	–0.0002(16)	–30.88
T(Si)	0.4801(3)	0.27873(19)	0.07792(14)	0.0064(6)	0.0116(7)	0.0099(6)	–0.0006(5)	–0.0013(4)	–0.0003(4)	–48.41
O1	0.2399(7)	0.4129(5)	0.0302(4)	0.0107(15)	0.0168(17)	0.0166(16)	0.0020(15)	–0.0013(11)	0.0025(12)	25.89
O2	0.6744(7)	0.2869(5)	0.4518(3)	0.0088(14)	0.0155(16)	0.0131(14)	0.0028(13)	0.0006(10)	0.0010(11)	27.34
O3	0.6892(7)	0.3470(5)	0.1947(3)	0.0087(14)	0.0210(18)	0.0115(14)	–0.0041(14)	–0.0009(10)	–0.0039(12)	26.81
O4	0.3136(7)	0.1070(5)	0.1406(4)	0.0106(14)	0.0118(14)	0.0170(15)	0.0005(14)	0.0000(11)	–0.0029(12)	27.69
ϕ (O5)	0.2009(7)	0.4123(5)	0.3325(4)	0.0076(14)	0.0212(18)	0.0160(15)	–0.0023(15)	–0.0020(11)	0.0001(12)	22.98

TABLE 5. REFINED STRUCTURAL OCCUPANCY OF CATION SITES IN GADOLINITE SAMPLES

Structural Site	SWC	Z2A
A (Yb^{3+}, 2)	46.2 electrons	43.6 electrons
M (Fe^{2+}, 1)	88(1)%	95(1)%
Q (Be^{2+}, 2)	90(2)%	94(1)%
Q (Si^{4+}, 2)	10(2)%	6(1)%
T (Si^{4+}, 2)	84(2)%	93(1)%
T (Be^{2+}, 2)	16(2)%	7(1)%

can disregard any significant datolite component. In order to estimate the hingganite component and a theoretical OH content, a second mineral formula recalculation was iteratively performed assuming a total of 10 total oxygen anions (including O from OH groups), (Si + Be) = 4, and M-site vacancy = 1 − (Fe + Ca) = 2 * H. The iteration was stopped when the total recalculated cations converged to a total positive charge of 20.000 (= 5 to 7 iterations). Results from this second normalization are presented in Table 6.

The compositional variations within each sample are illustrated by means of chondrite-normalized plots (Fig. 5a, b) and atom per formula unit (*apfu*) plots of the total LREE *versus* HREE (Fig. 5c), of the ratios Y/Yb *versus* Ce/Nd (Fig. 5d), and of the total *apfu* LREE *versus* Fe+Ca (Fig. 5e). Sample SWC shows the largest compositional variation and is typically LREE-dominant or slightly HREE-dominant, ranging from gadolinite-(Ce) to gadolinite-(Y), whereas sample Z2A is more homogeneous and identified as gadolinite-(Y) (Fig. 5, Table 6). Most of the variation in composition is seen in the REE content and is explained by a simple LREE ⇔ HREE exchange (Fig. 5c). The actinide contents of both samples are low, with UO_2 below detection limits and ThO_2 around 400 ppm in Z2A and slightly higher (between 0.05 and 0.49 wt.%) in SWC (Table 6; Supplementary Table 1); Pb is close to detection limit (<130 ppm) and up to 900 ppm. Calcium is present as a minor element in all samples. Totals for several analyses of sample SWC are somewhat low, around 97.5–99.9%, suggesting either a low estimate of BeO content or the presence of hydroxyl, although O–H stretching modes are not seen in the Raman spectra. A few EMP measurements including F indicate no significant F content, with values at or just above detection limit (<0.01 to 0.02 wt.%), except for less than 5% of all analyses yielding up to 0.68 wt.% F that correlate with a higher Ca content. Preliminary data including a much larger set of elements reveal the presence of trace Mn (~800 ppm), P (~500 ppm), Mg (~150 ppm), and Al (~130 ppm), whereas S, Nb, Ta, Ti, As, Sr, and K were not detected (< 50–100 ppm).

Laser ablation-inductively coupled plasma-mass spectrometry

The LA-ICP-MS measurements of sample WC-1A are given in Supplementary Table 2. The results reveal a small but significant B content varying from ~250 ppm up to ~690 ppm from LREE-rich to HREE-rich domains; the Be content increases slightly from ~3.5 to ~4.0 wt.%. The measured REE content is consistent with the EMP data. Uranium and Th yield 40–210 and 370–980 ppm, respectively. Other significant elements revealed by these LA-ICP-MS analyses and not analyzed by EMP include Mn (1154–1313 ppm), Zn (480–595 ppm), and 11 other elements below 100 ppm (Pb ~ 70 ppm, Al ~ 43 ppm, Mg ~ 42 ppm, Ti ~ 24 ppm, Rb ~ 15 ppm, K ~ 14 ppm, Sn ~ 10 ppm, Li ~ 8 ppm, and Bi, Sr, Ga ~ 5 ppm). All other elements analyzed are below 5 ppm or below detection limit (Supplementary Table 2).

Discussion

Variation of chemical compositions

Gadolinite from the White Cloud pegmatite is distinct in exhibiting a large variation in composition from LREE- to HREE-rich within a single occurrence, as well as variable Fe content (Fig. 5, Table 6). A chondrite-normalized plot of sample Z2A reveals a distinct enrichment in HREE+Y with variation in HREE content and a roughly similar LREE content (Fig. 5a). In contrast, all analyses of sample SWC show similar normalized LREE and HREE values on average and a variation of LREE content correlated with a decrease in HREE (Fig. 5b). All samples show a strong Eu anomaly (Fig. 5a, b) explained by feldspar crystallization during intrusion of the granite. While sample SWC has variable LREE content, sample Z2A has more consistent LREE and variable HREE content (Fig. 5c, d).

Most other REE-minerals in the pegmatite incorporate mostly LREE or HREE, but not both, such as for instance allanite-(Ce) and thalenite-(Y) (Raschke *et al*. 2018). Gadolinite with variable compositions has also been identified in other localities. Gadolinite-(Y) from Baveno and Cuasso al Monte in the Italian Southern Alps (Pezzotta *et al*. 1999) shows minor compositional variation, comparable to sample Z2A and to the gadolinite-(Y) from sample SWC (Fig. 5c, e). Gadolinite-(Y) from Miyazuma-kyo, Yokkaichi, Japan (Miyawaki *et al*. 1984), and other localities (Bačík *et al*. 2014) approaches the composition of sample Z2A. Gadolinite crystals in Bastnäs-type deposits from the Bergslagen mining region of south-central Sweden (Holtstam & Andersson 2007) show a similar variation from gadolinite-(Ce), -(Nd), and -(Y),

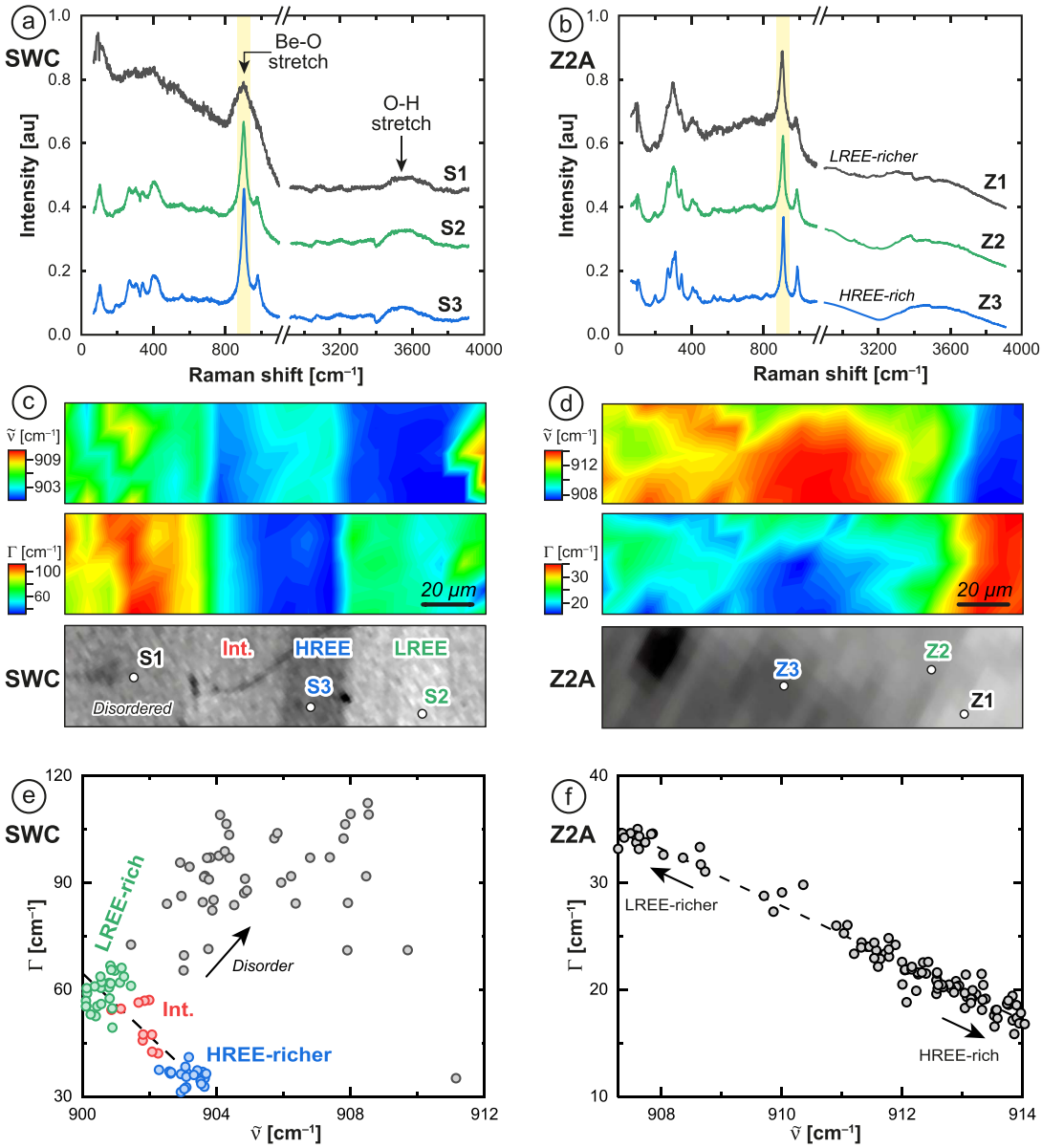

FIG. 3. Micro-Raman spectroscopy of thin sections of samples Z2A and SWC. (a, b) Representative Raman spectra of SWC and Z2A located in (c, d). Note the small but significant H_2O or OH response between 3000 and 3500 cm^{-1} clearly visible in the SWC samples and less evident in Z2A. (c, d) Lineshape analysis of tetrahedral Be–O stretch vibrations with spatial variation and correlation between peak position (ν), width (FWHM; Γ), and BSE image. (e, f) Correlated change of peak position and peak width of Be–O stretch vibration; an increase in LREE content leads to peak shifting (red-shift) and broadening in both samples, with a stronger peak broadening in SWC due to its higher LREE content. In sample SWC, poor quality Raman responses (gray dots) are attributed to stronger disorder, *e.g.*, "S1" in (a).

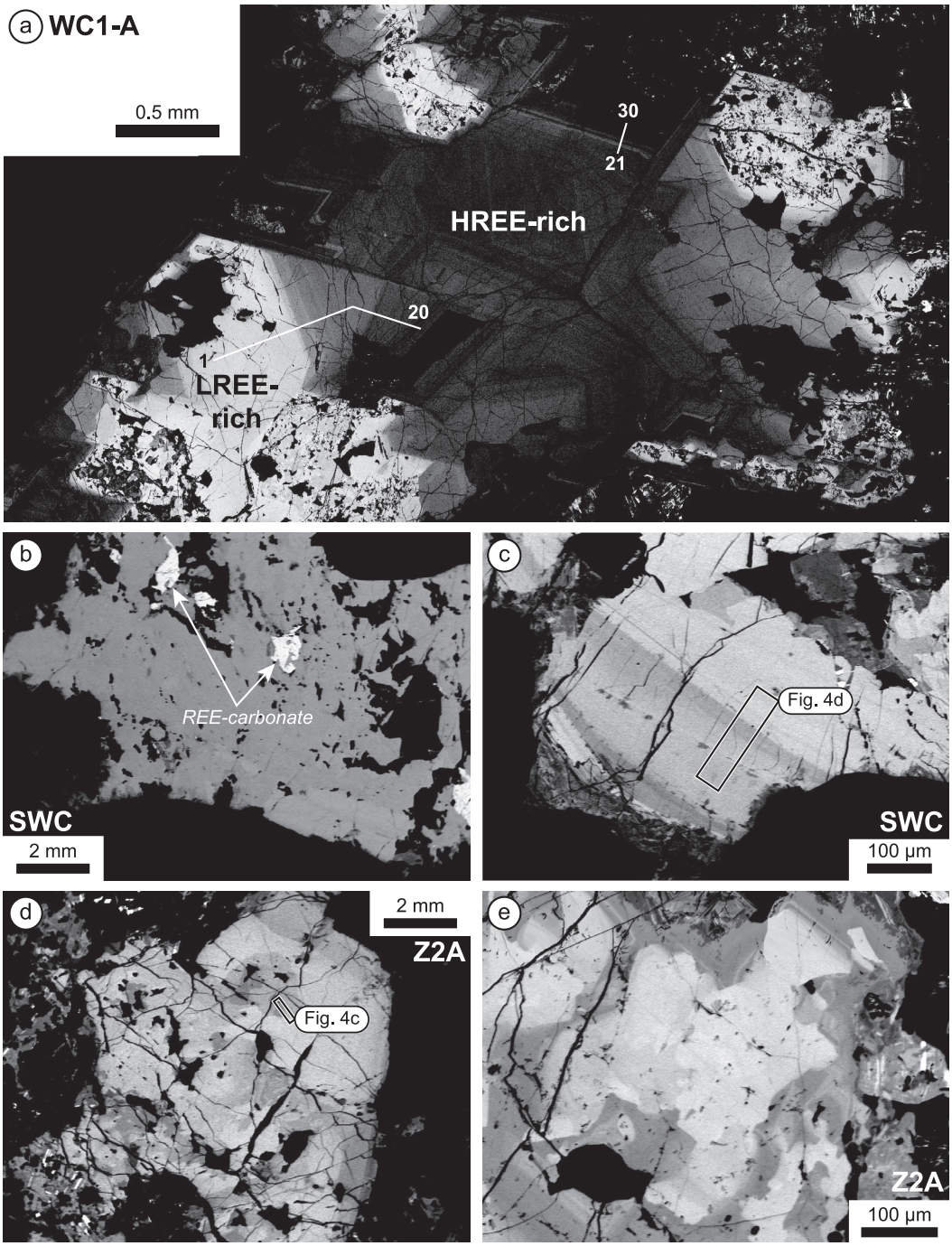

FIG. 4. High-contrast BSE images of gadolinite crystals in samples (a) WC1-A, (b, c) SWC, and (d, e) Z2A. The variation of grayscale correlates with richness in LREE (bright) or HREE (dark). White lines 1–20 and 21–30 in (a) indicate the position of LA-ICP-MS spot analyses. BSE images (c) and (d) are equivalent to Figure 2e, f and 2g, h, respectively.

TABLE 6. REPRESENTATIVE AVERAGE EMP ANALYSES OF GADOLINITE WITH MINERAL FORMULA RECALCULATION ASSUMING 10 OXYGEN ATOMS AND 4 Si + Be = 4, M-SITE VACANCY = 1 – (Fe+Ca), AND H = M-SITE VACANCY

	SWC					Z2A			
	VLow Y	Low Y	Med Y*	High Y	Vhigh Y	Low Y	Med Y	High Y	Vhigh Y
Points	5	3	7	7	3	5	7	5	4
SiO_2 (wt.%)	21.81	21.47	21.81	22.18	22.13	22.25	22.12	22.87	24.62
ThO_2	0.37	0.12	0.34	0.29	0.06	0.04	0.02	0.04	0.05
UO_2	0.01	< 0.01	0.04	0.08	< 0.01	< 0.01	< 0.01	< 0.01	0.02
FeO	10.17	11.31	11.74	11.88	12.04	12.23	12.39	12.74	13.02
CaO	0.25	0.11	0.21	0.19	0.15	0.09	0.08	0.12	0.19
Y_2O_3	6.76	9.98	10.88	14.22	19.56	18.70	20.18	24.47	28.50
La_2O_3	4.29	4.80	1.70	1.61	5.75	0.28	0.22	0.24	0.30
Ce_2O_3	18.26	16.65	11.98	9.98	11.29	2.33	1.72	1.70	1.93
Pr_2O_3	2.74	2.16	2.38	1.94	1.24	0.77	0.59	0.52	0.52
Nd_2O_3	10.40	7.81	10.40	8.46	4.04	6.10	5.06	3.95	3.19
Sm_2O_3	2.71	1.99	3.12	2.59	0.94	3.92	3.64	2.53	1.56
Eu_2O_3	0.08	0.08	0.09	0.11	0.15	0.06	0.11	0.11	0.13
Gd_2O_3	2.02	1.61	2.39	2.13	0.83	4.27	4.26	3.17	2.06
Tb_2O_3	0.48	0.38	0.57	0.52	0.24	0.97	0.97	0.72	0.51
Dy_2O_3	2.99	2.84	3.78	3.69	1.69	6.49	6.52	5.10	3.63
Ho_2O_3	0.50	0.56	0.68	0.74	0.39	1.24	1.25	1.08	0.83
Er_2O_3	1.88	2.30	2.57	2.85	1.86	4.13	4.21	3.84	3.34
Tm_2O_3	0.36	0.48	0.51	0.60	0.48	0.70	0.71	0.69	0.65
Yb_2O_3	2.80	4.07	4.15	5.06	4.87	4.64	4.73	5.04	5.30
Lu_2O_3	0.31	0.54	0.56	0.74	0.85	0.58	0.58	0.69	0.85
BeO**	8.76	8.94	8.87	9.00	9.34	9.16	9.21	9.42	9.60
H_2O**	1.18	0.71	0.45	0.49	0.56	0.45	0.38	0.36	0.50
Total	99.13	98.91	99.21	99.35	98.45	99.39	98.96	99.39	101.29
Si (*apfu*)	2.031	1.996	2.022	2.024	1.983	2.010	1.998	2.009	2.066
Be	1.969	2.004	1.978	1.976	2.017	1.990	2.002	1.991	1.934
Th	0.008	0.003	0.007	0.006	0.001	0.001	0.001	0.001	0.001
U	0.000	-	0.001	0.002	-	-	-	-	0.000
Fe	0.792	0.879	0.910	0.907	0.903	0.924	0.936	0.936	0.914
Ca	0.024	0.011	0.020	0.019	0.014	0.009	0.007	0.011	0.017
Y	0.335	0.494	0.537	0.691	0.933	0.899	0.970	1.144	1.272
La	0.147	0.165	0.058	0.054	0.190	0.009	0.007	0.008	0.009
Ce	0.622	0.567	0.406	0.333	0.370	0.077	0.057	0.055	0.059
Pr	0.093	0.073	0.081	0.065	0.040	0.025	0.020	0.017	0.016
Nd	0.346	0.259	0.344	0.276	0.129	0.197	0.163	0.124	0.096
Sm	0.087	0.064	0.100	0.082	0.029	0.122	0.113	0.077	0.045
Eu	0.003	0.003	0.003	0.003	0.004	0.002	0.003	0.003	0.004
Gd	0.062	0.050	0.073	0.064	0.025	0.128	0.127	0.092	0.057
Tb	0.015	0.012	0.017	0.016	0.007	0.029	0.029	0.021	0.014
Dy	0.090	0.085	0.113	0.109	0.049	0.189	0.190	0.144	0.098
Ho	0.015	0.017	0.020	0.021	0.011	0.035	0.036	0.030	0.022
Er	0.055	0.067	0.075	0.082	0.052	0.117	0.119	0.106	0.088
Tm	0.010	0.014	0.015	0.017	0.013	0.020	0.020	0.019	0.017
Yb	0.079	0.115	0.117	0.141	0.133	0.128	0.130	0.135	0.136
Lu	0.009	0.015	0.016	0.020	0.023	0.016	0.016	0.018	0.022
H	0.367	0.220	0.139	0.149	0.167	0.134	0.114	0.107	0.139
Total	7.160	7.112	7.052	7.056	7.094	7.060	7.058	7.047	7.025

* Analysis "Med Y" of SWC is representative of the crystal chip used for XRD analysis.

** BeO and H_2O are estimated *via* the mineral formula recalculation (see text for detail).

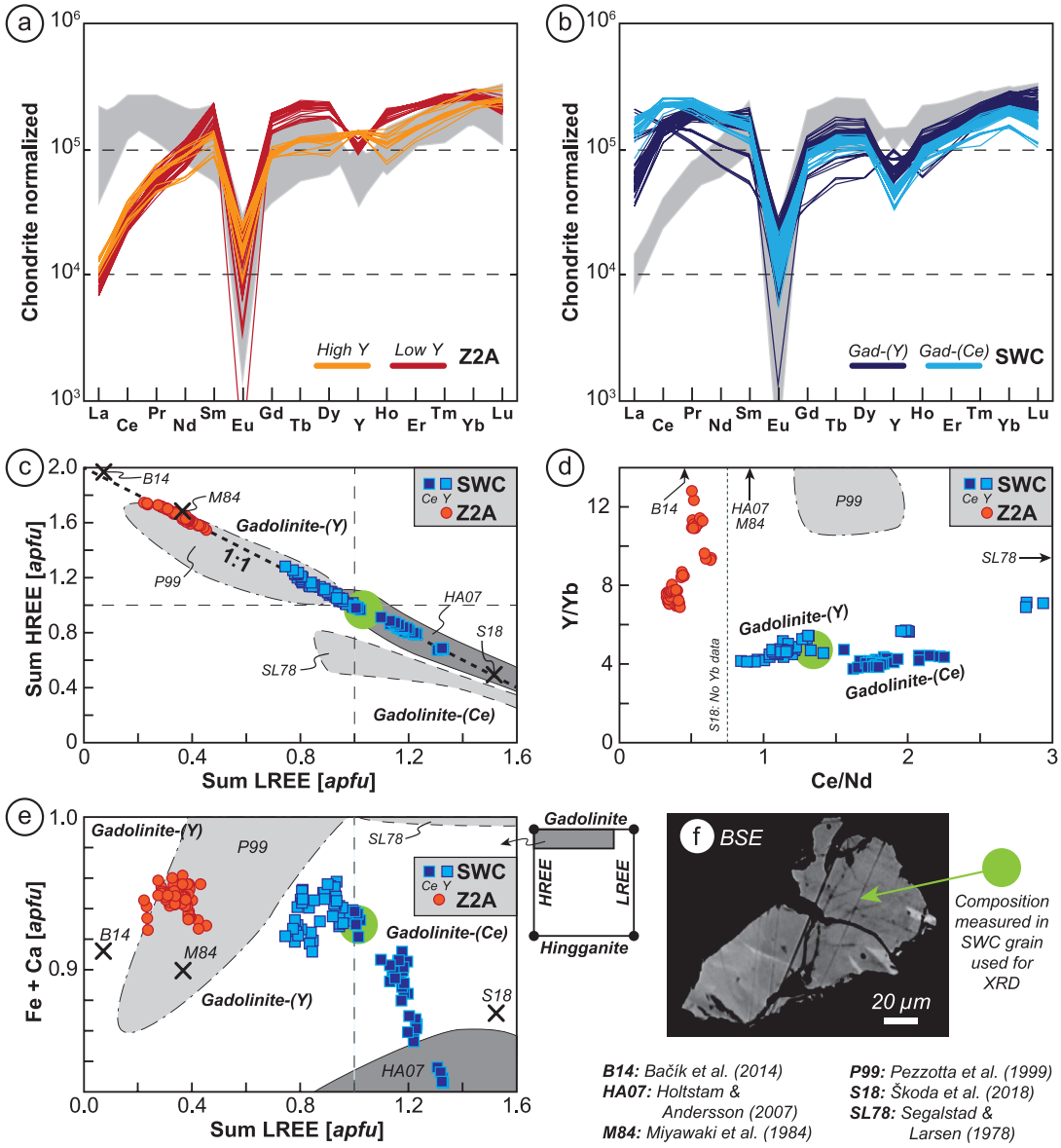

FIG. 5. Plots of EMP data for sample SWC (orange-red tones) and Z2A (blue tones). (a, b) Chondrite-normalized plots of major gadolinite zones containing similar chemical distributions (chondrite values from McDonough & Sun 1995). (c, d, e) Plots of EMP analyses highlighting variation of (c) total HREE *versus* total LREE (*apfu* = atom per formula unit), (d) Y/Yb *versus* Ce/Nd, and (e) Fe + Ca *versus* LREE (*apfu*). (f) BSE image of the crystal chip of SWC analyzed by XRD showing minimal variations of composition with a few small bright spots corresponding to a LREE-richer domain. A representative averaged composition for this grain is right at the transition from gadolinite-(Ce) to -(Y) (= "SWC Med Y" in Table 6). B14: Bačík *et al*. (2014); M84: Miyawaki *et al*. (1984); P99: Pezzotta *et al*. (1999); SL78: Segalstad & Larsen (1978); S18: Škoda *et al*. (2018); HA07: Holtstam & Andersson (2007).

as observed in sample SWC, yet with a higher Y/Yb ratio (Fig. 5d). Gadolinite crystals from Skien in the Norwegian southwestern Oslo region (Segalstad & Larsen 1978) have strong core-to-rim zonation, yet are still rich in LREE (Fig. 5c). Although an extensive discussion on this compositional variation is beyond the scope of this paper, the observed change in composition is likely related to the very late fractionation of the residual pegmatitic fluid from LREE-rich to HREE-rich (Fig. 4).

The EMP analysis of samples SWC and Z2A yielded 0.788–0.931 and 0.900–0.951 *apfu* Fe, respectively (Table 6; Supplementary Table 1). The XRD data support the relative amount of Fe in the two samples: at the M site, SWC has 0.87 *apfu* Fe and Z2A has 0.95 *apfu* (Table 5). These results suggest the presence of vacancies at the M site, especially in sample SWC. As B analysis by LA-ICP-MS yielded mostly less than 700 ppm (Supplementary Table 2), the datolite component can be ignored. Similarly, the herderite component is also ignored, as only ~500 ppm P was detected by EMP (Supplementary Table 1). No significant Li was detected by LA-ICP-MS (~8 ppm). Therefore, we suggest that the calculated vacancies at the M site chiefly represent a substitution towards hingganite, with a double hydroxylation of the φ-site compensating for the vacancy left by the divalent cation (*e.g.*, Demartin *et al*. 2001, Holtstam & Andersson 2007). The decrease in HREE and increase in LREE at the A site correlates with lower Fe^{2+} at the M site (Table 6, Fig. 5e), which is in agreement with Bačík *et al*. (2014). This observation suggests a preference for hydroxylation at higher LREE-content in gadolinite (Fig. 5e). The total REE cations at the A site is close to 2 *apfu* in most analyses (1.99 ± 0.03).

The cell parameters are among the largest reported for gadolinite minerals, with values similar to gadolinite-(Nd) (Škoda *et al*. 2018, Bačík *et al*. 2017). The A-M polyhedral layer expands to accommodate the LREE. This expansion correlates with the M-site vacancy (Fig. 5e). This is seen most prominently in expansion of the A polyhedron, from 24.74 $Å^3$ in Z2A to 26.26 $Å^3$, in SWC (Table 3a, b). Unlike the A-M layer, the Q-T layer exhibits only minor changes in polyhedral volumes as the larger A and M cation are accommodated by flexure of the tetrahedral rings of Si and Be (Fig. 1).

Electrostatic site potentials

Electrostatic energy potentials were calculated using the code ELEN (Smyth 1989) based on a nominal point charge model with charges of +3 for A, +2 for M and Q, +4 for T, and –2 for O1, O2, O3, O4, and φ (Table 4). For this calculation, the atoms at the split A-site were ignored. These potentials are useful for predictions of possible heterovalent substitutions as well as stable isotope fractionation. The Y site has a deep potential that varies inversely with site radius and is typical of REE and Y sites in minerals (Smyth & Bish 1988). The T site is typical of Si tetrahedral sites. The Q site has a deeper potential than typical Be tetrahedral sites that range from 28.9V for bromellite to 30.3V for phenacite M2. The M site is larger and has a shallower potential than typical Fe^{2+} sites. The oxygen site potentials are also typical of non-bridging oxygen sites in silicate minerals, and the non-silicate oxygen (φ) has the shallowest potential as do non-silicate oxygen positions in other silicate minerals (Smyth & Bish 1988).

Low hydroxyl content at the φ site

In the absence of iron and the presence of hydroxyl at the φ site, a solid solution with hingganite or datolite should form *via* the exchange $^{M}(Fe,Ca)^{+2} + {}^{\varphi}2O^{-2} \leftrightarrow {}^{M}\square + {}^{\varphi}2(F,OH)^{-1}$. Indeed, Raman spectra indicate the presence of a small amount of water or other OH species for both SWC and Z2A (Fig. 3). Similarly, Cámara *et al*. (2008) reported 0.29 *apfu* OH^{-1} at the φ site in gadolinite-(Y), and Škoda *et al*. (2018) documented a small OH^{-1} peak at 3525 cm^{-1} in gadolinite-(Nd) with 0.337 *apfu* OH^{-1} in their specimen.

We cannot entirely rule out the presence of minor F^{-1} instead of OH^{-1} at the φ site. Due to the low count rate on the EMP (low X-ray yield, strong absorption) and a strong overlap of F *K*α with Ce *M*ζ, the detection limit for F is high. Additional EMP analyses including F mainly yield values near the detection limit (<0.01 to 0.02 wt.%), and the rare abnormal high F-contents up to 0.68 wt.% F correlates with higher Ca values, which is likely due to either small fluorite inclusions or a secondary X-ray effect from the abundant surrounding fluorite. Fluorine is certainly abundant in the rock, yet it appears unlikely that a significant quantity of F substitutes at the φ site in the investigated samples.

The mineral formula recalculation suggests that possibly up to 0.11–0.14 *apfu* OH is present in sample Z2A, and values up to 0.37 *apfu* in SWC (Table 6; Supplementary Table 1). These values are only approximate, likely represent a maximum content, and are qualitatively consistent with the Raman observations. The accuracy of the recalculated water content depends heavily on the quality of the data and the correctness of all assumptions, including the oxidation state of each element (especially Fe) that can affect the charge balance. Nonetheless, they should not be too far from the truth, as all EPMA

analysis totals are between 98.5 and 101.5 wt.% (including the recalculated H_2O and BeO content), and no additional elements were found in significant quantity by LA-ICP-MS, although minor amounts of Mn, Zn, and B were identified (Supplementary Table 2).

Be–Si disorder

Sample SWC is the first documented case of significant Be–Si disorder in a mineral from XRD structural refinement. This is a robust conclusion because of the large difference in X-ray scattering between Be and Si. Demartin *et al*. (1993) suspected that this was a possibility and considered it in their analyses of gadolinite from various fissure and granitic pegmatite localities in the Alps but found no evidence of Be–Si disorder or substitution in their XRD data. Demartin *et al*. (2001) addressed Be–Si disorder, but due to the lack of convincing evidence at the time, used the absence of evidence as an assumption for their chemical formula calculations. Škoda *et al*. (2016) did observe minor Be–Si disorder (under 5%) in their analysis of gadolinite-(Nd), but they did not elaborate on this topic. The current data offer a robust indication of significant Be-Si disorder between crystallographically distinct tetrahedral sites.

The Q site of sample SWC has 88(2)% Be and 12(2)% Si, while the T site has 86(2)% Si and 15(2)% Be. The Q site of Z2A has 93(1)% Be and 7(1)% Si, and the T site has 94(1)% Si and 6(1)% Be (Table 5). The disordering of Si, and potential to have excess Si at the Q site, or deficient Si at the T site, indicates that one cannot assume 2 *apfu* for Si *a priori* when normalizing the chemical formula of gadolinite. However, a total of four Be + Si per formula unit is consistent with the XRD data for gadolinite. There is no evidence for vacancies at either the Q or T sites. The occupants are chiefly Si or Be, as LA-ICP-MS revealed less than 800 ppm B and ~8 ppm Li (Supplementary Table 2), which is consistent with the observation that the White Cloud Pegmatite and Pikes Peak Granite in general are depleted in B (Simmons & Heinrich 1980).

The Q and T site tetrahedra are very similar in volume and bond lengths, so they are fit for ionic substitutions (Table 3a, b). The Q sites of the samples have tetrahedral volumes of 2.27 $Å^3$ and 2.23 $Å^3$ for SWC and Z2A, respectively. The T sites of samples SWC and Z2A have volumes of 2.23 $Å^3$ and 2.21 $Å^3$, respectively, which is minimally less than that of the Q site. The Be tetrahedra are relatively undistorted, similar to the Si tetrahedra. Beryllium is a relatively rare element and not commonly analyzed due to analytical difficulty for light elements, so its presence in common rock-forming silicates, particularly layer and framework silicates, may be widely overlooked.

Conclusions

Gadolinite from the White Cloud pegmatite is structurally flexible and chemically variable, ranging from gadolinite-(Ce) to gadolinite-(Y) dominant members. The high variability in the LREE *versus* HREE contents between two distinct gadolinite samples and the observed chemical zonation within each gadolinite crystal reflect changing fluid or silica-rich liquid composition or other environmental parameters during REE crystallization. These specimens are also notable in that they have significant M-site vacancies, which are higher in the most LREE-rich domains, and very limited B. These vacancies are explained by the hydroxylation of the φ site with no evidence for a significant amount of F substituting for OH. Thus, there is a small but significant solid-state solution with hingganite, with very minimal component from datolite or other endmembers of the gadolinite supergroup.

Although beyond the scope of this paper, the enrichment of REE in the liquid could be explained through the process of constitutional zone refining (*e.g.*, London 2018), and the observed mineral chemistry could be the result of a final fractional crystallization of the residual liquid in the core of the pegmatite with an initial supersaturation of LREE and enrichment of the remaining liquid in HREE at undercooling conditions (London 2014). The mineralogy suggests that the mineralizing liquid was Si- and F-rich with limited Be, yet more work is required to constrain its exact composition.

The disorder of Be at the T site provides direct evidence that Be can substitute into Si tetrahedra. This Be–Si disorder could be present in more than only gadolinite minerals, due to the omnipresence of Si in tetrahedral coordination in minerals of the crust and upper mantle. If Be is able to substitute for Si, or even Al, it could be present in many rock-forming minerals as a trace element. Disorder could be found in other Be-silicates, such as phenakite, beryl, and euclase, and these are strong candidates for seeking Be–Si disorder in future studies. Since Be (or B) is not regularly analyzed for, its overall abundance and geochemical significance may not yet have been fully recognized.

Acknowledgments

This study was funded in part by grant NSF-EAR 1416979 to JRS, by the Bolyard Scholarship from the Rocky Mountain Association of Geologists to REH, and by a student fellowship from Mile High Rock and

Mineral Society to REH. JMA acknowledges funding from NSF EAR-1427626 and the University of Colorado Boulder for purchase of the JEOL JXA-8230 electron microprobe. We thank Dr. M. Guillong for providing the LA-ICP-MS analyses. We greatly appreciate comments and suggestions from the two reviewers, Dr. R. Škoda and Dr. W. Simmons, and from Guest Editor T. Martins.

References

Allaz, J.M., Williams, M.L., Jercinovic, M.J., Goemann, K., & Donovan, J. (2019) Multipoint background analysis: Gaining precision and accuracy in microprobe trace element analysis. *Microscopy and Microanalysis* **25**, 30–46.

Azavant, P. & Lichanot, A (1993) X-ray scattering factors of oxygen and sulfur ions: An *ab initio* Hartree-Fock calculation. *Acta Crystallographica* **(A)49**, 91–97.

Bačík, P., Fridrichová, J., Uher, P., Pršek, J., & Ondrejka, M. (2014) Crystal chemistry of gadolinite-datolite group silicates. *Canadian Mineralogist* **50**, 1–17.

Bačík, P., Miyawaki, R., Atencio, D., Cámara, F., & Fridrichová, J. (2017) Nomenclature of the gadolinite supergroup. *European Journal of Mineralogy* **29**, 1–16.

Cámara, F., Oberti, R., Ottolini, L., Della Ventura, G., & Bellatreccia, F. (2008) The crystal chemistry of Li in gadolinite. *American Mineralogist* **93**, 998–1004.

Černý, P. & Ercit, T.S. (2005) The classification of granitic pegmatites revisited. *Canadian Mineralogist* **43(6)**, 2005–2026.

Cromer, D.T. & Mann, J. (1968) X-ray scattering factors computed from numerical Hartree-Fock wave functions. *Acta Crystallographica* **(A)24**, 321–325.

Demartin, F., Pilati, T., Diella, V., Gentile, P., & Gramaccioli, C.M. (1993) A crystal-chemical investigation of Alpine gadolinite. *Canadian Mineralogist* **31**, 127–136.

Demartin, F., Minaglia, A., & Gramaccioli, C.M. (2001) Characterization of gadolinite-group minerals using crystallographic data only: The case of hingganite-(Y) from Cuasso al Monte, Italy. *Canadian Mineralogist* **39**, 1105–1114.

Donovan, J.J. & Tingle, T.N. (1996) An improved mean atomic number correction for quantitative microanalysis. *Journal of Microscopy* **2**, 1–7.

Farrugia, L.J. (2014) WinGX – Version 2014.1. An integrated system of windows programs for the solution, refinement and analysis of single crystal X-ray diffraction data. *Journal of Applied Crystallography* **45**, 849–854.

Gibson, S.J. & Ehlmann, A.J. (1970) Annealing characteristics of metamict gadolinite from Rode Ranch Texas. *American Mineralogist* **55**, 288–291.

Guillong, M., von Quadt, A., Sakata, S., Peytcheva, I., & Bachmann, O. (2014) LA-ICP-MS Pb-U dating of young zircons from the Kos-Nisyros volcanic centre, SE Aegean arc. *Journal of Analytical Atomic Spectrometry* **29**, 963–970.

Haynes, C.V. (1965) Genesis of the White Cloud and related pegmatites, South Platte Area, Jefferson County, Colorado. *Geological Society of America Bulletin* **76**, 441–462.

Holtstam, D. & Andersson, U.B. (2007) The REE minerals of the Bastnas-type deposits, South-Central Sweden. *Canadian Mineralogist* **45**, 1073–1114.

London, D. (2014) Subsolidus isothermal fractional crystallization. *American Mineralogist* **99**, 543–546.

London, D. (2018) Ore-forming processes within granitic pegmatites. *Ore Geology Reviews* **101**, 349–383.

McDonough, W.F. & Sun, S.-S. (1995) The composition of the Earth. *Chemical Geology* **120**, 223–253.

Miyawaki, R., Nakai, I., & Nagashima, K. (1984) A refinement of the crystal structure of gadolinite. *American Mineralogist* **69**, 948–953.

Nilssen, B. (1973) Gadolinite from Hundholmen, Tysfjord, North Norway. Contribution to the Mineralogy of Norway, No. 55. *Norsk Geologisk Tidskrift* **53**, 343–348.

Pezzotta, F., Diella, V., & Guastoni, A. (1999) Chemical and paragenetic data on gadolinite-group minerals from Baveno and Cuasso al Monte, southern Alps, Italy. *American Mineralogist* **84**, 782–789.

Raschke, M.B., Anderson, E.J.D., VanFosson, J., Allaz, J.M., Smyth, J.R., Škoda, R., Persson, P.M., & Becker, R. (2018) Rare-earth crystal chemistry of thalénite from different environments. *Mineralogical Magazine* **82**, 313–327.

Segalstad, T.V. & Larsen, A.O. (1978) Gadolinite-(Ce) from Skien, southwestern Oslo region, Norway. *American Mineralogist* **63**, 188–195.

Sheldrick, G.M. (2015) Crystal structure refinement with *SHELXL*. *Acta Crystallographica* **(C)71**, 3–8.

Simmons, W.B., Jr. & Heinrich, E.W. (1980) Rare earth pegmatites of the South Platte District, Colorado. *Colorado Geological Survey Research Series* **11**, 131.

Škoda, R., Plásil, J., Čopjaková, R., Novák, M., Jonsson, E., Galiová, V.M., & Holtstam, D. (2016) Gadolinite-(Nd), IMA 2016-013. *Mineralogical Magazine* **80**, 916.

Škoda, R., Plášil, J., Čopjaková, R., Novák, M., Jonsson, E., Galiová, M.V., & Holtstam, D. (2018) Gadolinite-(Nd), a new member of the gadolinite supergroup from Fe-REE deposits of Bastnäs-type, Sweden. *Mineralogical Magazine* **82**, 133–145.

Smith, D.R., Noblett, J., Wobus, R.A., Unruh, D., Douglass, J., Beane, R., Davis, C., Goldman, S., Kay, G.,

GUSTAVSON, B., SALTOUN, B., & STEWART, J. (1999) Petrology and geochemistry of late-stage intrusions of the A-type, mid-Proterozoic Pikes Peak Batholith (Central Colorado, USA): Implications for petrogenetic models. *Precambrian Research* **98**, 271–305.

SMYTH, J.R. (1989) Electrostatic characterization of oxygen sites in minerals. *Geochimica et Cosmochimica Acta* **53**, 1101–1110.

SMYTH, J.R. & BISH, D.L. (1988) *Crystal Structures and Cation Sites of the Rock-Forming Minerals*. Allen & Unwin, Boston, Massachusetts, United States.

Received October 26, 2019. Revised manuscript accepted March 6, 2020.